Tunable Large-scale Compressive Strain Sensor Based on Carbon Nanotubes/PDMS Foam Composites by Additive Manufacturing

*Chao Liu, Linh Le, Mingshao Zhang, Junjun Ding**

Chao Liu, Junjun Ding
Kazuo Inamori School of Engineering
New York State College of Ceramics
Alfred University
Alfred, NY 14802, USA
E-mail: dingj@alfred.edu

Linh Le
Flextrapower, Inc.
29-10 Thomson Avenue, Fl 7th
Long Island City, NY 11101, USA

Mingshao Zhang
Department of Mechanical and Mechatronics Engineering
School of Engineering
Southern Illinois University Edwardsville
Edwardsville, IL 62026, USA

Keywords: polymer-matrix composite, foam, additive manufacturing, strain sensor, carbon nanotubes

Abstract

The compressive strain sensor is an extensively-used flexible electronic device because of its capability to convert mechanical deformation to an electrical signal. However, the difficulty in tuning the performance of the strain sensor limits its further applications. Herein, we present the approach of fabricating a carbon nanotube (CNT)/ polydimethylsiloxane (PDMS) compressive

strain sensor, which has both tunable mechanical and electrical performance. CNT plays the role of reinforcement due to its outstanding mechanical strength and electrical conductivity; PDMS is a widely-used matrix because of its softness and nontoxicity. We use the material extrusion 3D printing (ME3DP) method to fabricate the composites, due to its advantages of design flexibility and compatibility with liquid-based materials. The foam microstructure formed by removing sodium chloride provides a large-scale deformation of at least 50% compressive strain and excellent elasticity. The strain sensor works durably over 10000 cycles, with a gauge factor of 17.4. We are also able to test the compressive strain sensor in detecting both large- and small-scale human motions due to the tunability of CNT/PDMS composites.

1. Introduction

Flexible electronics, such as stretchable supercapacitor,[1] wearable strain sensor,[2] flexible electrode,[3] and semiconductor,[4] have developed rapidly in recent years. As a typical flexible electronic device, strain sensors are widely used as human motion detectors, accurate pulse wave monitors, or force sensors due to their ability to convert physical deformation to the electrical resistance change.[5] Compared with tensile strain sensors, compressive strain sensors are frequently used for piezoresistivity, pressure, and gas sensing.[5e, 6] Conventional methods are used to fabricate strain sensors. For example, Wang et al. used electrospinning method to build carbon black (CB) reinforced thermoplastic polyurethane (TPU) matrix composites for ultrathin strain sensors. [7] Jia et al. achieved composite films by spraying Ag microparticles and MXene on the waterborne polyurethane (WPU) layers.[8] Hu et al. also used spray coating method to fabricate CB/ polydimethylsiloxane (PDMS) strain sensors by spraying CB solution on the sacrificial polyvinyl alcohol (PVA) layer.[9] Chang et al. summarized the fabrication methods of transparent strain sensors, which include casting, solution evaporation and ink jetting.[10] While these methods have the advantages of high manufacturing speed and large-batch manufacturing, the simplicity of these methods limits their applications in fabricating sophisticated strain sensors.

Additive manufacturing (AM), also called 3D printing, has recently received greater attention, due to its ability to fabricate complex 3D structures with the advantages of design flexibility, low cost, and small-batch production.[11] AM can use various of print materials such as viscous ink, solid filament, and powder, as well as different fabrication methods, such as layer-by-layer extrusion, photopolymerization, direct energy deposition, and material jetting methods. The conventional AM approaches include fused deposition modeling (FDM),[12] direct ink writing (DIW),[13] robocasting,[14] stereolithography (SLA),[15] digital light processing (DLP),[16] PolyJet,[17] electron beam melting (EBM),[18] and selective laser sintering (SLS).[19] Cutting-edge 3D printing methods have also been used for manufacturing. For examples, Kelly et al. developed volumetric

additive manufacturing method to fabricate small and soft materials which could be attached on other objects.[20] Oran et al. used the approach of implosion fabrication to build micro-scale and patterned 3D scaffold structures.[21] Rohbeck et al. used two-photon lithography laser-based method to fabricate micro-scale metamaterials.[22] In particular, material extrusion 3D printing (ME3DP) is a method used to build 3D prototypes by extruding materials layer by layer. ME3DP is a configurable approach to fabricate elastic strain sensors by extruding viscosity inks. For example, Liu et al. demonstrated a strain sensor with hybrid double-network hydrogels by pressure-controlled DIW.[23] Also, carbon-based ink has been 3D printed with a liquid-based extrusion technique to fabricate a strain sensor by Muth et al..[24] Further, Kim et al. produced an eutectic gallium–indium (EGaIn) alloy strain sensor using the DIW approach.[25]

Silicone rubber polydimethylsiloxane (PDMS) has been broadly used in soft devices and bio applications due to its flexibility, biocompatibility, nontoxicity, and moldability.[11a, 26] Although PDMS has excellent stretchability with more than 100% strain elongation,[1a] over 3 MPa compressive stress is needed to compress a solid PDMS bulk for 50% strain, inhibiting its applications in the compressive strain sensors.[27] The foam structure provides notable deformability for PDMS, due to its macro and micropores in the scaffold structure.[28] Another limitation of PDMS on its further applications is nonconductivity. To improve the performance issues of these pure substances, the fabrication of composites is a commonly used method. Recently, research has shown that the electrical performance of PDMS is enhanced by fabricating nanocomposites with reinforced conductive carbon materials. For example, carbon nanofiber,[29] carbon nanotubes,[30] and carbon black[31] were used as reinforcements to improve the electrical conductivity of PDMS by fabricating nanocomposites. Also, the property of composites is controllable by tuning the ratio of reinforcement and matrix materials. For example, Jung et al. demonstrated the electrical conductivity of the CNT/PDMS composite was controlled by adjusting the CNT concentration.[32] While much research has focused on the properties of carbon material/PDMS composites, little work has been done on achieving the controllable performance of CNT/PDMS nanocomposites with a foam structure by the ME3DP method.

In this work, we present the fabrication of a large-scale compressive strain sensor with CNT/PDMS foam composites by the ME3DP approach. The mechanical and electrical performance of PDMS is both improved by using CNTs as reinforcement. The foam microstructure fabricated by the ME3DP method and removed sacrificial sodium chloride (NaCl) demonstrates superior elasticity and compressibility for at least 50% strain. The electrical conductivity and gauge factor of the strain sensor is controllable by adjusting the concentration of CNT. The strain sensor is sufficiently durable to work for at least 10000 cycles and obtains the maximum gauge factor of 17.4.

Applications of the compressive strain sensor were fabricated by mounting the printed samples on the insole and computer mouse to detect both large- and small-scale human motions.

2. Results and Discussion

2.1. Rheology and Composition of Inks

Extrudable inks can acquire a shear-thinning property via the ME3DP approach, meaning the viscosity of extruded ink decreases as the shear rate increases. Therefore, we need to measure the essential rheological properties of inks for 3D printing. The viscosity of composite materials is determined by both the matrix and the reinforcement. Pure PDMS Sylgard 184 is a Newtonian fluid with stable viscosity as the shear rate changes, which is shown as the curve of 0:10 ratio in **Figure 1**(c). However, the Newtonian fluid is unable to hold the shape of the prototype printed by ME3DP. Therefore, we mixed the high-viscosity PDMS SE 1700 with PDMS 184 at the weight ratio of 7:3 to achieve a non-Newtonian matrix with the shear-thinning property, which is demonstrated as the curve of 7:3 ratio in **Figure 1**(c). The viscosity of the ink is also affected by NaCl. Since the average particle size of NaCl is ~10 μm, the NaCl considerably increases the viscosity and inhibits extrusion. Consequently, we added silicone oil and glycerol to adjust the viscosity for an extrudable ink. It should be noted that the silicone oil, with its polymerized siloxane chemical composition, is similar to PDMS we used, and thus is an appropriate choice to dilute the mixture. The viscosity of ink distinctly decreases after adding silicone oil at 25 wt% of NaCl. Trace of glycerol (8 wt% of NaCl) was infilled to adjust the viscosity associated with silicone oil and also contribute to the formation of the model, due to its ability to improve the plasticity. All viscosity curves of ink with 1-5 wt% CNT demonstrate the shear-thinning property, which is shown in **Figure 1**(d), indicating their capability to form a model by the ME3DP method. PDMS molecule chains intertwine with van der Waals force in the static state at a low shear rate (0.01-5 s^{-1}). Viscosity of the composite increases from 1 to 3 wt% CNT concentration, because CNTs are infilled between PDMS molecule chains. Nevertheless, the viscosity decreases after more CNTs are loaded from 3 to 5 wt% concentration because the entanglement of PDMS molecule chains is dramatically reduced by excessive CNTs. Hence, at a low shear rate, the viscosity first increases and decreases as the CNT concentration increases from 1 to 5 wt%, which is presented in **Figure 1**(e). At a high shear rate (5-100 s^{-1}), since most PDMS molecule chains are separated due to a greater applied shear force, the viscosity of the composites is predominately attributable to the concentration of CNT. Therefore, the viscosity increases as the CNT concentration increases from 1 to 5 wt% at a high shear rate, as shown in **Figure 1**(e).

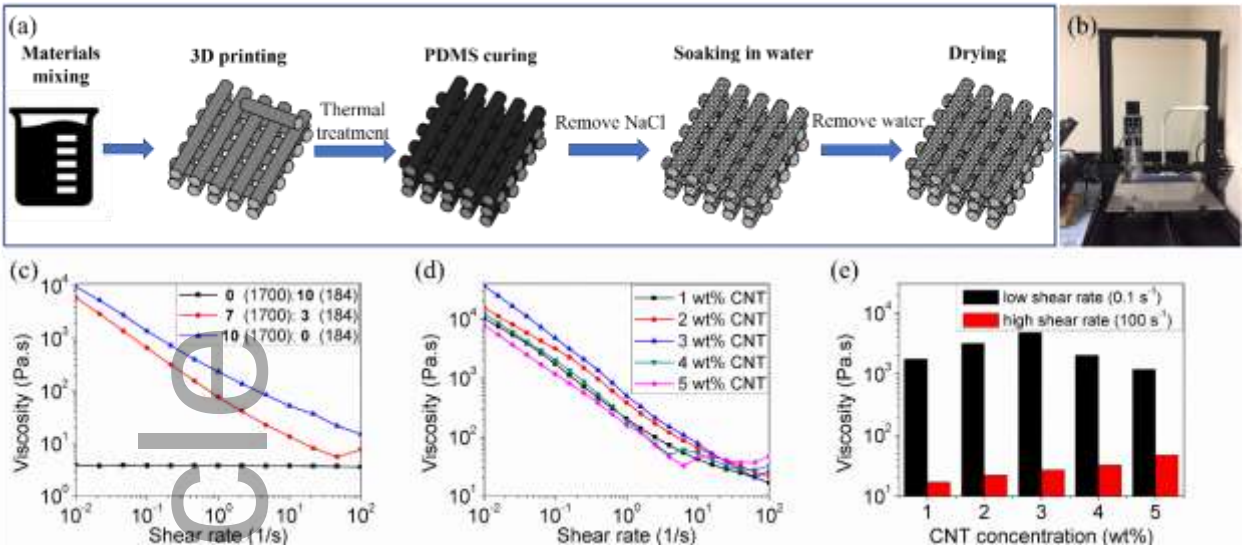

Figure 1. (a) Schematic illustration of the whole fabrication process, including materials mixing, 3D printing, PDMS curing, soaking in water and drying. (b) The custom-made ME3DP printer. (c) The viscosity of the mixture of PDMS SE 1700 and Sylgard 184 at 0:10, 7:3, and 10:0 weight ratios. (d) The viscosity of inks with 1-5 wt% CNT at a shear rate from 0.01 s^{-1} to 100 s^{-1}. (e) The viscosity vs. CNT concentration at a low shear rate of 0.1 s^{-1} and a high shear rate of 100 s^{-1}.

2.2. 3D Printing Process and Microstructure of the Structure

To obtain a large-scale compressible deformation, we designed a scaffold model rather than a solid structure, as exhibited in **Figure 2**(a). The interval between lines on the same layer is equal to the line width (600 μm, **Figure 2**(b)), allowing sufficient space for the broadening of lines during compression. The cylindrical lines in the printing head collapsed into an elliptic shape due to the rheological property of the viscous ink. Therefore, we adjusted the layer height as 200 μm (**Figure 2**(c)), smaller than the line width, to compensate for the collapse of ink and maintain the firm attachment between adjacent layers. To ensure the NaCl can be entirely removed by water, we needed to achieve an open-cell foam. The foam microstructure is influenced by the amount of NaCl, which is shown in **Figure 2**(d, e). The microvoid density of the foam structure with a lower NaCl ratio (PDMS: NaCl = 1:1) is smaller than the ones with a higher NaCl ratio (PDMS: NaCl = 1:1.3). The structure with higher NaCl concentration has a higher cavity content, allowing more liquid paths to remove NaCl microparticles and construct the open-cell foam structure. Residual NaCl microparticles, marked with yellow circles in **Figure 2**(d), are found in the CNT/PDMS foam composites fabricated with a lower NaCl ratio. In comparison, no remaining NaCl microparticles are found in the foam composites fabricated with a higher NaCl ratio, as shown in **Figure 2**(e). It is also observed that the higher concentration of NaCl facilitates the formation of the open-cell foam structure. Higher magnification of the structure (**Figure 2**(f)) shows that CNTs, which are pointed

out by red arrows, are wrapped in PDMS with no apparent CNT aggregations, suggesting that CNTs disperse uniformly in the PDMS matrix.

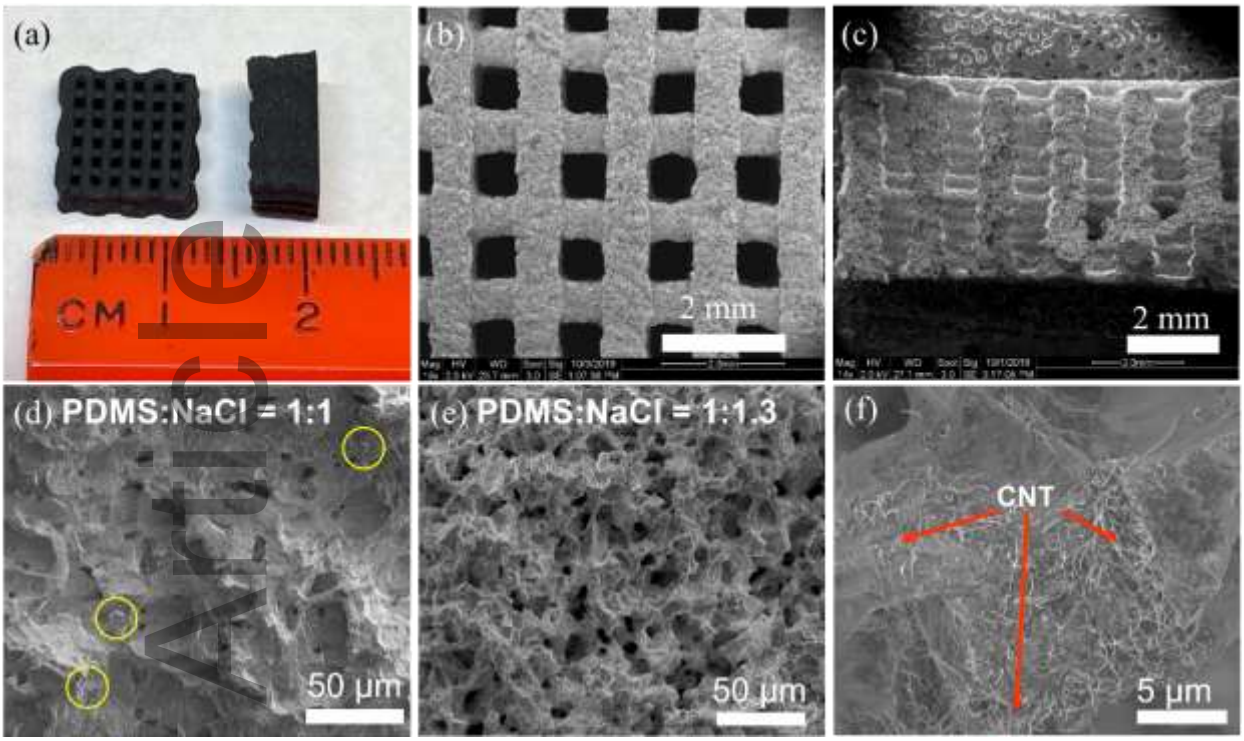

Figure 2. (a-c) Optical, top-view SEM, and cross-sectional SEM images of the 3D printed scaffold structure, respectively. Cross-sectional SEM images of 4 wt% CNT printed samples of (d) 1:1 and (e) 1:1.3 PDMS to NaCl weight ratio, respectively. The yellow circles in (d) mark residual NaCl particles. (f) High magnification SEM image of (e) shows uniform dispersion of CNTs (pointed out by red arrows) in PDMS.

2.3. Mechanical Performance of Compressive Strain Sensors

A well-performed strain sensor requires excellent mechanical properties such as large-scale deformation and resilience. We performed cyclic compressive testing at 50% strain up to 100 cycles on samples with 0-5 wt% CNT concentrations. As shown in **Figure 3**(a), the scaffold structure could be compressed to 50% strain and recover to its original condition, showing the extraordinary elasticity of the foam structure. The stress-strain curve of the 4 wt% CNT sample, shown in **Figure 3**(b), demonstrates hysteresis loops and can be observed in open-cell foams.[33] The linear behavior at 0-25% strain, containing the linear elastic and the plateau regions with Young's modulus of ~700 kPa, results from the compression of the microvoids and the deformation microvoids walls.[28] The densification region at 25-50% strain with a steeply increasing slope is due to over-compaction of microvoids.[34] In **Figure 3**(c), the hysteresis loop of the 1st cycle exhibits a slight 3.5% strain loss due to plastic deformation; the 10th, 25th, 50th, and 100th hysteresis loops show no plastic deformation, suggesting the exceptional structural robustness. As shown in **Figure 3**(d), the

hysteresis loops of samples at strain rates of 1-8% s^{-1} overlap thoroughly, which indicates the structure attains outstanding resilience for rapid deformation. The influence of CNT concentration on mechanical properties is shown in **Figure 3**(e, f). The Young's modulus and maximum stress stabilize over 100 compressive cycles. Due to the excellent mechanical strength of CNT, Young's modulus of composite improves from ~800 kPa with 0 wt% CNT to ~2500 kPa with 5 wt% CNT. The maximum stress, however, decreases from ~96% with 0 wt% CNT to ~86% with 5 wt% CNT because of the stiff structure of CNT. Nonetheless, our structure still displays excellent elasticity due to the retention of 86% maximum stress.[35]

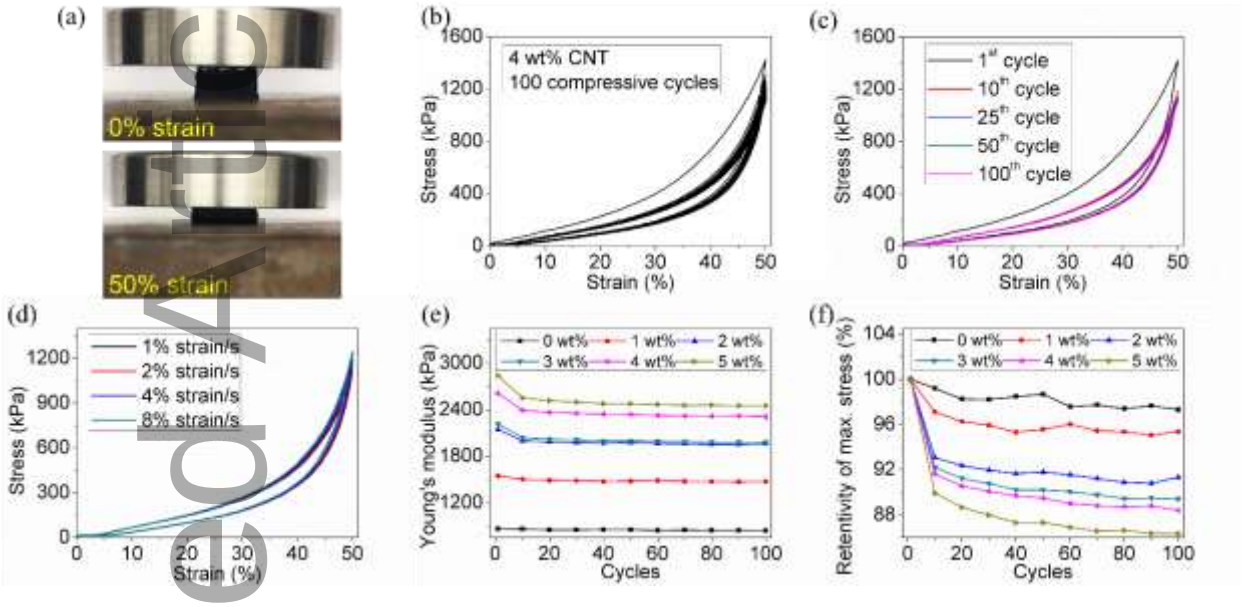

Figure 3. (a) Compressive testing at origin and 50% strain. The stress vs. strain curves of 4 wt% CNT sample in (b) complete 100 cycles, (c) 1st, 10th, 25th, 50th, and 100th specific cycles, and (d) 6th-10th cycles compressed at the speed of 1, 2, 4, and 8% strain s^{-1}. (e) The change in Young's modulus of 0-5 wt% CNT samples throughout 100 cycles. (f) The change in retentivity of maximum stress of 0-5 wt% CNT samples under 100 cycles.

2.4. Electromechanical Performance of Compressive Strain Sensors

The large-scale foam structure CNT/PDMS composites provide not only exceptional elasticity and compressibility but also remarkable electrical conductivity. The compressed sample with 5 wt% CNT has a maximum conductivity of 8.3×10^{-3} S m^{-1}, which is approximately 3 orders of magnitude higher than the same sample without deformation. To investigate the influence of CNT concentration on the electrical performance of the strain sensor, we performed the electromechanical testing at 50% strain deformation in 10000 cycles. The relative change in resistance ($\Delta R/R_0 = (R_0-R)/R_0$, where R_0 and R are the electrical resistance without and with deformation, respectively) of samples with 3-5 wt% CNT increases as the CNT concentration increases, as shown in **Figure 4**(a). The $\Delta R/R_0$ of samples with 0-2 wt% CNT is omitted in the

figure because of the nonconductivity. High CNT concentrations lead to the increase of interconnections between adjacent CNTs in the PDMS matrix, thereby increasing electrical conductivity pathways. In this case, the higher concentration of CNT leads to higher electrical sensitivity of the composites. Moreover, considering samples with different CNT concentration separately, the $\Delta R/R_0$ increases in the initial cycles before stabilizing; this stability is maintained for at least 10000 cycles. Samples with higher CNT concentration requires fewer compressive cycles to reach the stabilized condition, suggesting that CNTs contribute to the stabilization process. The maximum gauge factor (GF) of our strain sensor is calculated at 5% strain of 5 wt% CNT sample (Figure S1, Supporting Information), which is GF=17.4. The performance of our strain sensor is compared with other research, as shown in **Table 1**. Our 3D printed strain sensor shows large sensing range and excellent cyclic stability. The sensitivity (evaluated by GF) of our strain sensor is better than or similar to the values in reported works.

Table 1. The performance of various polymer-based compressive strain sensors.

Material	Fabrication method	GF	Sensing rage (%)	Stability (cycle)	Reference
Pt/PDMS	Ultraviolet curing	11.45	0-2	10000	[5e]
Nanoclay/CB/TPU	DIW 3D printing	4.7	0-80	>1000	[6]
Coated CNT/PDMS	DIW 3D printing	~2	0-90	1000	[28]
Graphene Foam/PDMS	Vacuum infiltration	~28	0-30	1000	[36]
Graphene Foam/PDMS	Dip-coating	~19	0-30	>500	[37]
Graphene Aerogel/PDMS	Vacuum infiltration	~1	0-80	20	[38]
CNT/PDMS	ME3DP	17.4	0-50	10000	This work

The percolation threshold of our CNT/PDMS foam composites is between 2 and 3 wt% CNT; a sample with 2 wt% CNT shows nonconductivity, while a sample with 3 wt% CNT demonstrates conductivity. Two foaming mechanisms, including foaming action and volume expansion, account for the percolation threshold of foam composites.[39] The foaming action represents the influence of the alignment of surrounded reinforcement of cells on the percolation. The volume expansion represents the influence of the localization of the reinforcement within the cell wall on the percolation. In our case, there is no foaming action effect, because the NaCl particles fill up the microvoids. There is also no volume expansion effect, because the transitional NaCl is uniformly mixed with CNT/PDMS composites before 3D printing. We attribute the increase of the percolation

threshold to the removal of the sacrificial material (NaCl). The adding of well-dispersed NaCl does not influence the percolation threshold of CNT/PDMS nanocomposites. However, the removal of the NaCl changes the CNT distribution. Interconnected CNTs that initially attached to the NaCl particles become disconnected after the NaCl is removed, leading to the decrease of interconnections of CNTs and the pathways of electrical conductivity. **Figure 4**(b) displays a microvoid after the removal of NaCl particles and the remaining CNTs inside. Therefore, the percolation threshold of our CNT/PDMS foam composites (2-3 wt% CNT) is higher than CNT/PDMS solid samples in other works.[30, 40]

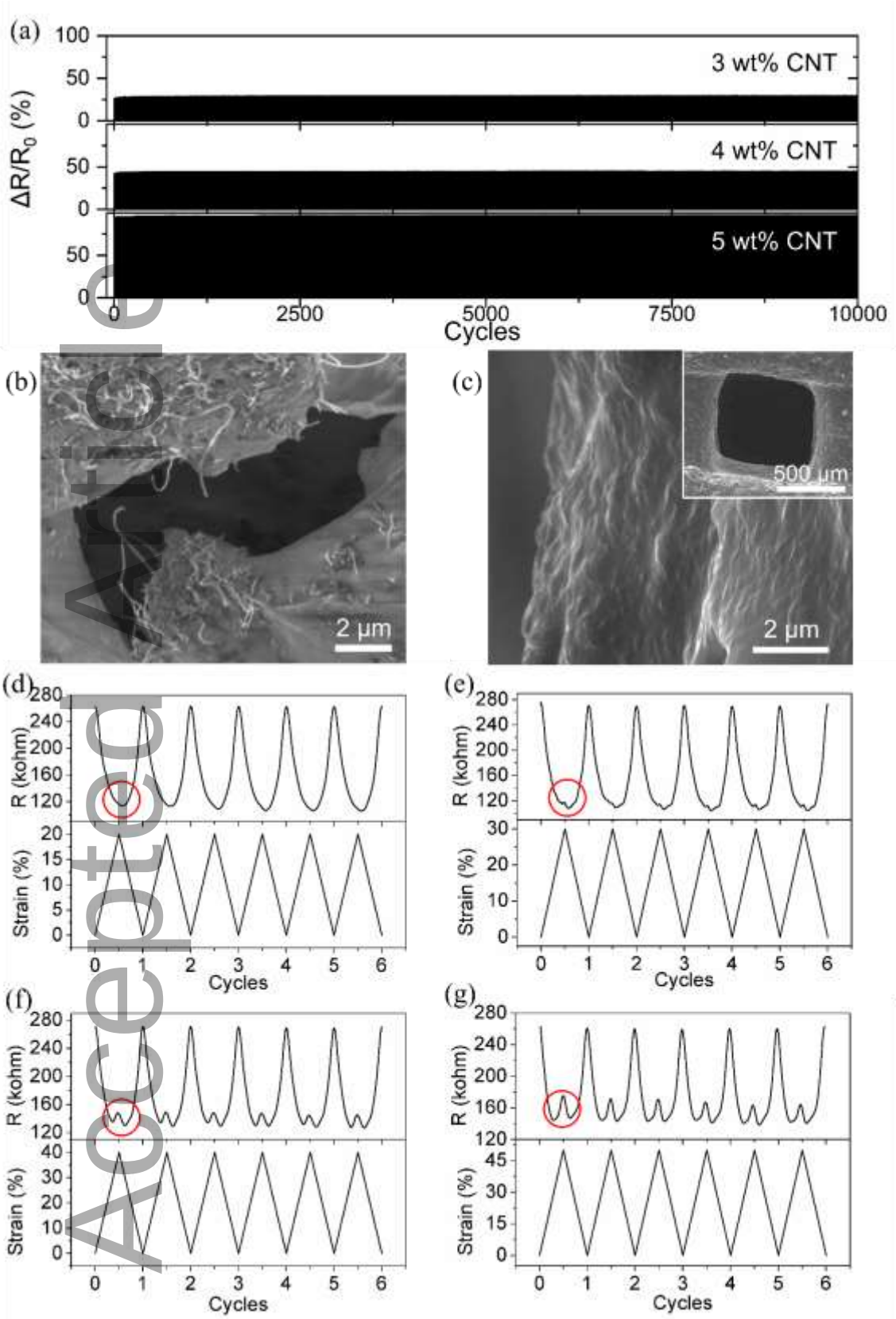

Figure 4. (a) The relative change in electrical resistance of 3-5 wt% CNT samples under 10000 compressive cycles. (b) SEM image of a microvoid in the foam structure. (c) SEM image of the wall in the millimeter void due to 3D printed architecture. Inset image shows an intact millimeter

void. (d-g) The electrical resistance at 20-50% strain in the initial 6 cycles with four different 4 wt% CNT samples, respectively.

Furthermore, in **Figure 4**(d-g), we observed the oscillation of the electrical resistance, meaning that the resistance decreased at a small strain but increased at a large strain (the oscillation of resistance is marked in red circles). We attribute the oscillation to the interconnection and separation of CNTs extend into the microvoids, shown in **Figure 4**(b). It should be note that millimeter voids due to 3D printed architecture have little effect on the oscillation because fewer CNTs extend into the millimeter voids, which is shown in **Figure 4**(c). **Figure 5** illustrates the compression of a microvoid with extending CNTs. As the microvoid becomes narrower in the initial 20% compressive strain from Ⅰ to Ⅱ, the number of interconnections between CNTs located on opposite of the microvoids walls increases. The pathways of electrical conductivity thus increase, while electrical resistance decreases. As the microvoid is further compressed at 20-50% strain from Ⅱ to Ⅲ, the interconnection of CNTs reaches a maximum, followed by increasing separation of connected CNTs due to their segregated distribution at the surface of the microvoid; as a result, electrical pathways decrease and electrical resistance increases. The degree of separation is proportional to the compressive strain, causing the increase of the resistance continuously. This result corresponds to the densification region (25-50% strain) in the mechanical analysis in which the microvoid is over-compressed.

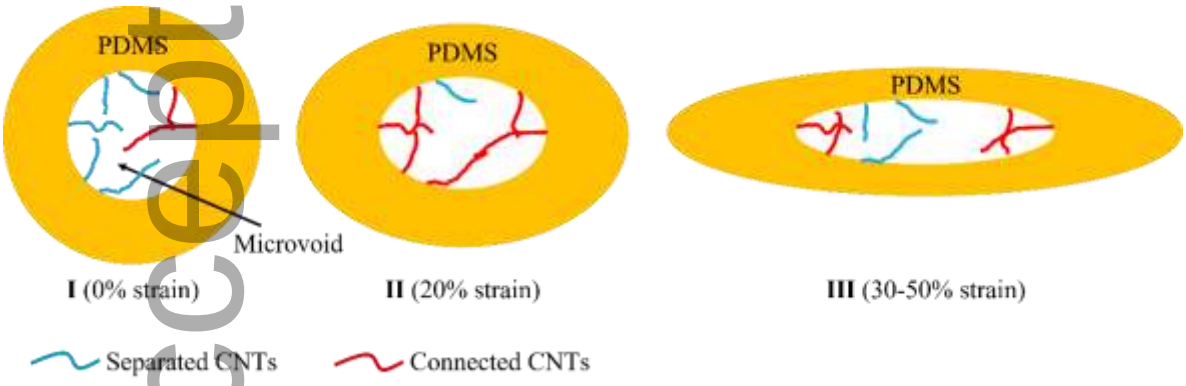

Figure 5. Schematic illustration of compression of a microvoid into which CNTs extend.

2.5 Applications of Compressive Strain Sensor to Detect Human Motions.

As presented above, our CNT/PDMS compressive strain sensor demonstrates robust mechanical resilience and outstanding electrical conductivity, which enables the strain sensor to detect human motions. Since the electromechanical property of the strain sensor can be tuned by adjusting the concentration of CNT, the sensitivity of the strain sensor can be tuned for different motion-detecting applications according to the scale of physical deformation. The quantitative analysis of

relative changes in electrical resistance was conducted on samples with 3 wt% and 5 wt% CNT to determine the impact of sensitivity on the performance of the strain sensor. As shown in **Figure 6**(a-c), the CNT/PDMS strain sensors were attached to an insole using conductive carbon and copper tapes and packaged in a sandwich structure to monitor walking, running, and jumping behaviors. It should be noted that walking and running behaviors achieved similar maximum $\Delta R/R_0$ values on both samples with 3 wt% CNT (**Figure 6**(d), $\Delta R/R_0$ ~ 40%) and with 5 wt% CNT (**Figure 6**(e), $\Delta R/R_0$ ~ 90%) because of the similar scale of compressive deformation. Instead of viewing the maximum $\Delta R/R_0$, the wave pattern, which includes frequency and wave shape, could be observed to differentiate walking and running behaviors. The maximum $\Delta R/R_0$ of jumping behavior, causing a larger compressive deformation, on the sample with 3 wt% CNT ($\Delta R/R_0$ ~ 60%) is 20% higher than the walking behavior on the same sample. On the other hand, the maximum $\Delta R/R_0$ of jumping behavior on the sample with 5 wt% CNT ($\Delta R/R_0$ ~ 90%) is approximately equal to the walking behavior on the same sample, because it reaches the saturation region. The results indicated that samples with lower electrical sensitivity are more suitable for detecting large-scale human motions that cause large deformation. The sample with a higher concentration of CNT and sensitivity reaches saturation quickly, inhibiting its capability to detect a larger strain.

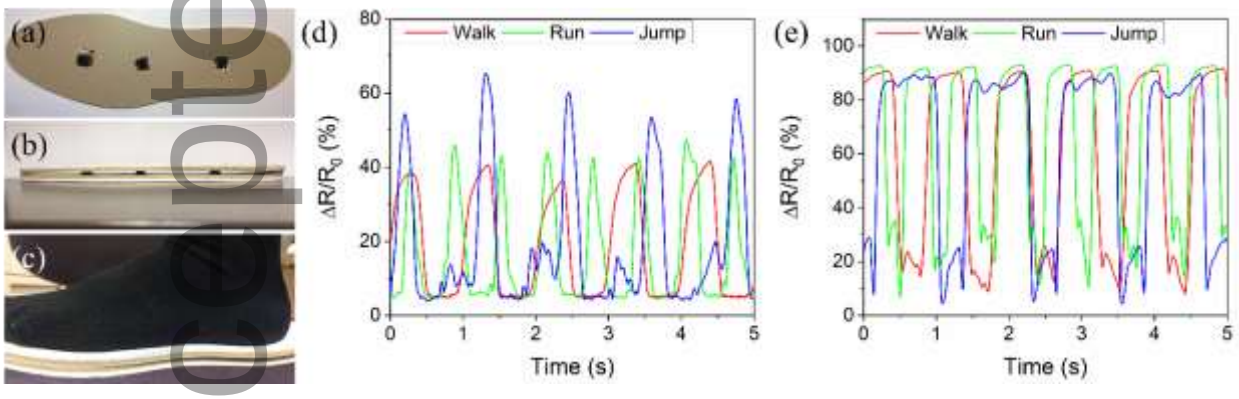

Figure 6. (a) The 3D printed CNT/PDMS foam samples were mounted on an insole. (b) A sandwich structure was built to pack the strain sensors. (c) Foot stepped on the sandwich structure to detect walking, running, and jumping behaviors. (d) The relative change in electrical resistance ($\Delta R/R_0$) of the sample with 3 wt% CNT related to behaviors. (e) $\Delta R/R_0$ of the sample with 5 wt% CNT related to behaviors.

Moreover, we explored another application by mounting our strain sensors onto a computer mouse to detect wrist motions shown in **Figure 7**(a). When the wrist was bent, the strain sensor was compressed, resulting in deformation. The sensors R_1 and R_2 were used to monitor turning the wrist

leftwards and rightwards, respectively. The sensor R_3 was used to monitor turning the forearm upwards and downwards. **Figure 7**(b-d) shows the relative change in resistance of samples with 3 wt% and 5 wt% CNT before and after bending the wrist. Compared with little change of $\Delta R/R_0$ among samples with 3 wt% CNT, a significant increase of $\Delta R/R_0$ is observed among samples with 5 wt% CNT after turning the wrist. Unlike stepping on the insole, turning the wrist induced much smaller deformation of the strain sensor. In this case, the sample with higher sensitivity is more appropriate to detect small-scale joint motions. Consequently, our CNT/PDMS compressive strain sensor can detect both large-scale and small-scale human motions, and we believe it has further applications in wearable devices and healthcare areas.

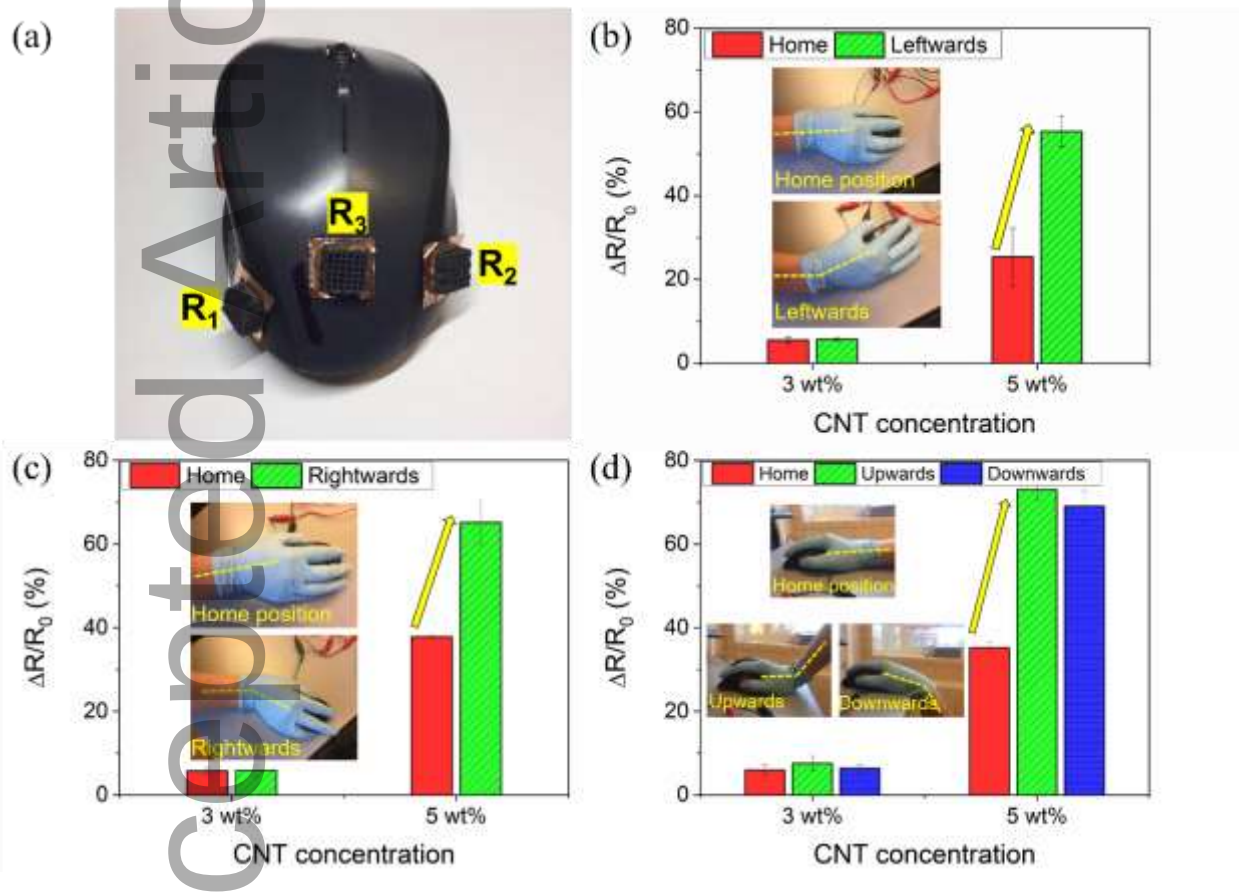

Figure 7. (a) The 3D printed samples were mounted on a computer mouse. The $\Delta R/R_0$ was measured on samples with 3 wt% and 5 wt% CNT with the movements of turning the wrist (b) leftwards, (c) rightwards, and (d) upwards and downwards.

3. Conclusions

In this study, we have fabricated a large-scale compressive strain sensor based on CNT/PDMS foam composites by the ME3DP method. CNTs were used as reinforcement to improve both the mechanical and electrical properties of PDMS. The foam microstructure built by sacrificial NaCl provided excellent elasticity which ranges in 50% strain deformation. The strain sensor worked stably in at least 10000 cycles with the maximum GF=17.4. The percolation threshold of

CNT/PDMS composites increases after the removal of sacrificial NaCl particles. The oscillation of electrical resistance at high compressive strain is found because of the densification of microvoids. The sensitivity of the strain sensor can be easily adjusted by modifying the CNT concentration. Thus, we fabricated devices of the compressive strain sensor by attaching 3D printed scaffold foam samples to the insole and computer mouse to detect both large-scale and small-scale human motions, respectively. We believe that our approach of applying CNT/PDMS composites to tune the properties of the strain sensor broadens the potential on the fabrication of flexible strain sensors, supercapacitors, semiconductors, and other soft electronic devices. Our approach of applying additive manufacturing to form the model also expends the routes of fabrication in a more flexible design and cost-saving method.

4. Experimental Methods

4.1. Materials: Multi-walled carbon nanotubes (MWCNTs, powder, 94% purity) were purchased from Graphene Supermarket (graphene-supermarket.com). PDMS SE 1700 and PDMS Sylgard 184 were obtained from Dow Corning. Sodium chloride (NaCl, powder, >99% purity), glycerol (>99.5% purity), and silicone oil were purchased from Alfa Aesar.

4.2. Ink Preparation: The composite was composed with a PDMS matrix and CNT reinforcement. The viscoelastic PDMS matrix was prepared by mixing high-viscosity PDMS SE 1700 and low-viscosity Sylgard 184. Initially, two elastomers were blended with their cross-linkers (10:1 weight ratio) separately. A vacuum desiccator was used to remove air bubbles before mixing PDMS SE 1700 and Sylgard 184 at a weight ratio of 7:3. MWCNTs were added at 0-5 wt% of the PDMS mixture. To obtain fine and homogeneous particles, NaCl was ball-milled using a PM 200 planetary ball mill (Retsch) with 5 mm zirconia grinding media at the speed of 300 rpm for 8 h. This ball-milled NaCl, with an average diameter of ~10 μm, was then added as an intermediate material to fabricate the foam structure. Glycerol and silicone oil were added to control the viscosity. The schematic illustration of the whole process is depicted in **Figure 1**(a).

4.3. Rheological Analysis: Rheology of ink was measured using a DISCOVERY HR-2 hybrid rheometer (TA Instruments) with a 40 mm diameter parallel plate at 25 °C, with a gap of 800 μm. The viscosity was measured via rotational flow sweep at a shear rate from 0.01 s^{-1} to 100 s^{-1}.

4.4. Materials Extrusion 3D Printing: A customized liquid-based 3D printer was modified from a commercial CR-10S FDM 3D printer (Creality), as shown in **Figure 1**(b). The strain sensor model was designed as a scaffold structure, with dimensions of 10×10×5 mm, using the SketchUp (Trimble) 3D modeling software. The STL file from the SketchUp was converted to a GCODE file for 3D printing by Ultimaker Cura slicer software. Inks were loaded into a syringe attached with a nozzle with an inner diameter of 600 μm. A stepper motor controlled the syringe to extrude the ink

at a printing speed of 3 mm s^{-1} at room temperature. The line width was set as 600 μm, equal to the nozzle size, for the sufficient printing feed. The layer height was set as 200 μm, slightly smaller than the line width, to compensate for the collapse of ink. Printed samples were cured in a thermal oven at 90 °C for 5 h, then immersed in deionized water for 3 days to remove NaCl. The sample was then dried at 120 °C for 1 day.

4.5. Characterizations: The morphologies and microstructures of samples were investigated using the Quanta 200F scanning electron microscope (SEM, FEI). We used the 5566 Universal Testing Machine (Instron) to evaluate the cyclic mechanical performance for 100 cycles at the compressive speed of 2.5, 5, 10, and 20 mm min^{-1}. A 2831E multimeter (BK Precision) was used to measure the electrical resistance by the two-point method between the top and bottom surface of the sample. A copper foil was used to decrease the contact resistance between 3D printed samples and the multimeter probes. The electrical conductivity (σ) is calculated as follows:

$$\sigma = \frac{H}{RA} \quad (1)$$

where H and A are the height and cross-sectional area of the scaffold sample, respectively, and R is the electrical resistance. The gauge factor (GF) is calculated as follows:

$$GF = \frac{(R_0 - R)/R_0}{\varepsilon} \quad (2)$$

where R_0 is the electrical resistance without deformation at room temperature, R is the electrical resistance with compressive deformation, and ε is the compression strain.

Acknowledgments

This work is sponsored by Fuzehub Jeff Lawrence Innovation Fund Manufacturing Grant, Gia Lam Urban Development and Investment Company Limited, Vingroup and supported by Vingroup Innovation Foundation (VINIF) under project code DA123_15062019. The authors thank Dr. Xingwu Wang for the suggestions on electrical testing. The authors are also thankful to Dr. Hyojin Lee for the help of rheology measurement. The authors also thank James Thiebaud for the advice on mechanical testing.

Conflict of Interest

The authors declare no conflict of interest.

References

[1] a) R. Zhang, J. Ding, C. Liu, E.-H. Yang, ACS Appl. Energy Mater. **2018**, 1, 2048; b) A. Ramadoss, K.-Y. Yoon, M.-J. Kwak, S.-I. Kim, S.-T. Ryu, J.-H. Jang, J. Power Sources **2017**, 337, 159.

[2] a) M. Amjadi, A. Pichitpajongkit, S. Lee, S. Ryu, I. Park, ACS Nano **2014**, 8, 5154; b) C. Wang, K. Xia, M. Jian, H. Wang, M. Zhang, Y. Zhang, J. Mater. Chem. C **2017**, 5, 7604.

[3] a) J. Ding, S. Fu, R. Zhang, E. Boon, W. Lee, F. T. Fisher, E.-H. Yang, Nanotechnology **2017**, 28, 465302; b) J. Ding, F. T. Fisher, E.-H. Yang, J. Vac. Sci. Technol. B **2016**, 34, 051205.

[4] a) L. Petti, N. Münzenrieder, C. Vogt, H. Faber, L. Büthe, G. Cantarella, F. Bottacchi, T. D. Anthopoulos, G. Tröster, Appl. Phys. Rev. **2016**, 3, 021303; b) Z. Wang, L. Peng, Z. Lin, J. Ni, P. Yi, X. Lai, X. He, Z. Lei, Sci. Rep. **2017**, 7, 1.

[5] a) T. Yamada, Y. Hayamizu, Y. Yamamoto, Y. Yomogida, A. Izadi-Najafabadi, D. N. Futaba, K. Hata, Nat. Nanotechnol. **2011**, 6, 296; b) H. Liu, Y. Li, K. Dai, G. Zheng, C. Liu, C. Shen, X. Yan, J. Guo, Z. Guo, J. Mater. Chem. C **2016**, 4, 157; c) S. Ryu, P. Lee, J. B. Chou, R. Xu, R. Zhao, A. J. Hart, S.-G. Kim, ACS Nano **2015**, 9, 5929; d) T. Yang, X. Jiang, Y. Zhong, X. Zhao, S. Lin, J. Li, X. Li, J. Xu, Z. Li, H. Zhu, ACS Sens. **2017**, 2, 967; e) C. Pang, G.-Y. Lee, T.-i. Kim, S. M. Kim, H. N. Kim, S.-H. Ahn, K.-Y. Suh, Nat. Mater. **2012**, 11, 795.

[6] P. Wei, H. Leng, Q. Chen, R. C. Advincula, E. B. Pentzer, ACS Appl. Polym. Mater. **2019**, 1, 885.

[7] X. Wang, X. Liu, D. W. Schubert, Nanomicro Lett **2021**, 13, 1.

[8] Y. Jia, Y. Pan, C. Wang, C. Liu, C. Shen, C. Pan, Z. Guo, X. Liu, Nanomicro Lett **2021**, 13, 1.

[9] M. Hu, Y. Gao, Y. Jiang, H. Zeng, S. Zeng, M. Zhu, G. Xu, L. Sun, Adv. Compos. Hybrid Mater. **2021**, 4, 514.

[10] a) X. Chang, L. Chen, J. Chen, Y. Zhu, Z. Guo, Adv. Compos. Hybrid Mater. **2021**, 4, 435; b) E. Roh, B.-U. Hwang, D. Kim, B.-Y. Kim, N.-E. Lee, ACS Nano **2015**, 9, 6252.

[11] a) C. Liu, L. Jiang, J. Ding, in ASME 2018 International Mechanical Engineering Congress and Exposition, Vol. 2, American Society of Mechanical Engineers Digital Collection, Pittsburgh, PA November, **2018**, 1; b) B. P. Conner, G. P. Manogharan, A. N. Martof, L. M. Rodomsky, C. M. Rodomsky, D. C. Jordan, J. W. Limperos, Addit. Manuf. **2014**, 1, 64.

[12] a) H. Mei, Z. Ali, I. Ali, L. Cheng, Adv. Compos. Hybrid Mater. **2019**, 2, 312; b) X. Xia, X. Xu, C. Lin, Y. Yang, L. Zeng, Y. Zheng, X. Wu, W. Li, L. Xiao, Q. Qian, ES Mater. Manuf. **2020**, 7, 40.

[13] B. Wang, Z. Zhang, Z. Pei, J. Qiu, S. Wang, Adv. Compos. Hybrid Mater. **2020**, 3, 462.

[14] L. Tabard, V. Garnier, E. Prud'Homme, E.-J. Courtial, S. Meille, J. Adrien, Y. Jorand, L. Gremillard, Addit. Manuf. **2021**, 38, 101776.

[15] J. Wang, Y. Liu, Z. Fan, W. Wang, B. Wang, Z. Guo, Adv. Compos. Hybrid Mater. **2019**, 2, 1.

[16] C. J. Thrasher, J. J. Schwartz, A. J. Boydston, ACS Appl. Mater. Interfaces **2017**, 9, 39708.

[17] M. D. Islam, H. Al Yassi, M. Dong, D. S. Choi, I. Seok, C. Liu, Z. Guo, J. E. Ryu, Eng. Sci. **2019**, 6, 86.

[18] S. M. J. Razavi, B. Van Hooreweder, F. Berto, Addit. Manuf. **2020**, 36, 101426.

[19] T. D. Ngo, A. Kashani, G. Imbalzano, K. T. Nguyen, D. Hui, Compos. B. Eng. **2018**, 143, 172.

[20] B. E. Kelly, I. Bhattacharya, H. Heidari, M. Shusteff, C. M. Spadaccini, H. K. Taylor, Science **2019**, 363, 1075.

[21] D. Oran, S. G. Rodriques, R. Gao, S. Asano, M. A. Skylar-Scott, F. Chen, P. W. Tillberg, A. H. Marblestone, E. S. Boyden, Science **2018**, 362, 1281.

[22] N. Rohbeck, R. Ramachandramoorthy, D. Casari, P. Schürch, T. E. Edwards, L. Schilinsky, L. Philippe, J. Schwiedrzik, J. Michler, Mater. Des. **2020**, 195, 108977.

[23] S. Liu, L. Li, ACS Appl. Mater. Interfaces **2017**, 9, 26429.

[24] J. T. Muth, D. M. Vogt, R. L. Truby, Y. Mengüç, D. B. Kolesky, R. J. Wood, J. A. Lewis, Adv. Mater. **2014**, 26, 6307.

[25] S. Kim, J. Oh, D. Jeong, W. Park, J. Bae, Soft Robot. **2018**, 5, 601.

[26] a) M. P. Wolf, G. B. Salieb-Beugelaar, P. Hunziker, Prog. Polym. Sci. **2018**, 83, 97; b) V. Ozbolat, M. Dey, B. Ayan, A. Povilianskas, M. C. Demirel, I. T. Ozbolat, ACS Biomater. Sci. Eng. **2018**, 4, 682.

[27] W. Lee, K. Yeo, A. Andriyana, Y. Shee, F. M. Adikan, Mater. Des. **2016**, 96, 470.

[28] Q. Chen, J. Zhao, J. Ren, L. Rong, P. F. Cao, R. C. Advincula, Adv. Funct. Mater. **2019**, 29, 1900469.

[29] S. Wu, J. Zhang, R. B. Ladani, A. R. Ravindran, A. P. Mouritz, A. J. Kinloch, C. H. Wang, ACS Appl. Mater. Interfaces **2017**, 9, 14207.

[30] K. Sun, P. Xie, Z. Wang, T. Su, Q. Shao, J. Ryu, X. Zhang, J. Guo, A. Shankar, J. Li, Polymer **2017**, 125, 50.

[31] X. Niu, S. Peng, L. Liu, W. Wen, P. Sheng, Adv. Mater. **2007**, 19, 2682.

[32] H.-C. Jung, J.-H. Moon, D.-H. Baek, J.-H. Lee, Y.-Y. Choi, J.-S. Hong, S.-H. Lee, IEEE. Trans. Biomed. Eng. **2012**, 59, 1472.

[33] L. J. Gibson, M. F. Ashby, Cellular solids: structure and properties, Cambridge Univ. Press, Cambridge, UK **1997**.

[34] a) C. Wu, X. Huang, X. Wu, R. Qian, P. Jiang, Adv. Mater. **2013**, 25, 5658; b) Y. Qin, Q. Peng, Y. Ding, Z. Lin, C. Wang, Y. Li, F. Xu, J. Li, Y. Yuan, X. He, ACS Nano **2015**, 9, 8933; c) K. H. Kim, Y. Oh, M. Islam, Nat. Nanotechnol. **2012**, 7, 562; d) Q. Chen, P. F. Cao, R. C. Advincula, Adv. Funct. Mater. **2018**, 28, 1800631.

[35] L. Qiu, J. Z. Liu, S. L. Chang, Y. Wu, D. Li, Nat. Commun. **2012**, 3, 1.

[36] Y. A. Samad, Y. Li, A. Schiffer, S. M. Alhassan, K. Liao, Small **2015**, 11, 2380.

[37] Y. A. Samad, Y. Li, S. M. Alhassan, K. Liao, ACS Appl. Mater. Interfaces **2015**, 7, 9195.

[38] Q. Zhang, X. Xu, H. Li, G. Xiong, H. Hu, T. S. Fisher, Carbon **2015**, 93, 659.

[39] A. Ameli, M. Nofar, C. Park, P. Pötschke, G. Rizvi, Carbon **2014**, 71, 206.

[40] J. Hwang, J. Jang, K. Hong, K. N. Kim, J. H. Han, K. Shin, C. E. Park, Carbon **2011**, 49, 106.

Table of Contents

CNT reinforced PDMS matrix foam composites are fabricated by material extrusion 3D printing method. The composites work as a compressive strain sensor and exhibit excellent elasticity and stability. The mechanical and electrical properties of the strain sensor can be tuned by the concentration of CNT in the composites. Applications of the compressive strain sensor demonstrate the capability in detecting both large-scale and small-scale human motions.

Chao Liu, Linh Le, Mingshao Zhang, Junjun Ding*

Tunable Large-scale Compressive Strain Sensor Based on Carbon Nanotubes/PDMS Foam Composites by Additive Manufacturing